Supporting Information

Charge Confinement and Thermal Transport Processes in Modulation-Doped Epitaxial Crystals (MoDECs) Lacking Lattice Interfaces

Elizabeth Radue[1], Evan L. Runnerstrom[2,3], Kyle P. Kelley[2,3], Christina M. Rost[1], Brian F. Donovan,[4] Everett D. Grimley[2], James M. LeBeau[2], Jon-Paul Maria[2,3], Patrick E. Hopkins[1,5,6,*]

1. Department of Mechanical and Aerospace Engineering, University of Virginia, Charlottesville, VA 22904, USA
2. Department of Materials Science, North Carolina State University, Raleigh, NC 27695, USA
3. Department of Materials Science and Engineering, Penn State University, State College, PA 16801, USA
4. Department of Physics, United States Naval Academy, Annapolis, MD 21402, USA
5. Department of Materials Science and Engineering, University of Virginia, Charlottesville, VA 22904, USA
6. Department of Physics, University of Virginia, Charlottesville, VA 22904, USA

Dr. E. Radue, Dr. C.M. Rost, Prof. P.E. Hopkins
Department of Mechanical Engineering and Aerospace Engineering
University of Virginia
122 Engineers Way, Charlottesville, VA 22904 USA

Dr. E.L. Runnerstrom, Prof. J. P. Maria
Department of Materials Science and Engineering
Penn State University
215 Steidle Building, University Park, PA 16802

Dr. E. D. Grimley, Prof. J. M. LeBeau
Department of Materials Science and Engineering
911 Partners Way FB I
Raleigh, NC 27695, USA

Prof. B.F. Donovan
United States Naval Academy
Department of Physics
572c Holloway Road, Annapolis, MD 21402

*Author to whom correspondence should be addressed: phopkins@virginia.edu

S1. Time domain thermoreflectance measurements

TDTR is an optical pump-probe measurement technique that, in our case, utilizes the output of a Ti:Sapphire oscillator that outputs laser pulses at 80 MHz centered at 1.55 eV (800 nm) with ~10.5 nm bandwidth. The output pulse train from the oscillator is split into a pump path and a probe path. The pump pulse-train is modulated with an electro-optic modulator, and then energetically doubled to 3.1 eV (400 nm) with a BiBO crystal[1] before being focused on the sample surface. The probe pulses are sent down a variable delay stage, and then focused coaxially with the pump using an infinity corrected objective lens. At the sample surface, the pump and probe spot sizes are focused to 19.0 and 9.0 $1/e^2$ radii, respectively. The modulated pump beam creates a frequency dependent heating event (at 8.8 MHz), from which the change in probe reflectivity is locked into. A thin aluminum transducer (nominally 80 nm) deposited on the surface of the samples serves to convert the absorbed photonic excitation into a temperature rise on the time scale of the electronic relaxation in the metal (< 10 ps), thus allowing our data to be representative of the probe reflectivity change due to temperature perturbations (i.e., change in reflectivity related to the temperature reflectance coefficient, or thermoreflectance), instead of having to consider the nonequilibrium carrier/plasma component to the change in the reflectivity (i.e., the free carrier reflectance coefficient).[2] We confirm the thickness of the Al transducer to within +/-3 nm using picosecond acoustics at the location in which TDTR measurements of thermal conductivity were conducted.[3-4]

The TDTR data, an example which can be seen in Fig. S1a, were analyzed using a cylindrically symmetric multilayer heat equation that accounts for both the frequency dependent pump modulation frequency and the pump-probe time delay, as described in the literature.[5-6] This model solves for the temperature rise on the surface of the Al film as a function of pump-probe delay time based on the thermal properties of each layer. Thus, the model is sensitive to the heat capacities and thermal conductivities of each material (Al, CdO, Al_2O_3) and the thermal boundary conductances at each of the materials' interfaces. We assume literature values for the thermal conductivity of the sapphire substrate, and determine the thermal conductivity of the Al film from converting 4-point probe measurements of electrical resistivity to thermal conductivity via the Wiedemann-Franz Law. The heat capacities of the Al , CdO, and sapphire were taken from the literature.[7-10] Thus, we fit our model to the data by adjusting the thermal conductivity for the CdO and the thermal boundary conductance across the Al/CdO interface until a best fit is achieved. At these thicknesses, we find that we are relatively insensitive to the thermal boundary conductance across the CdO/sapphire interface, as shown by the sensitivity curves[11] in Fig. S1b.
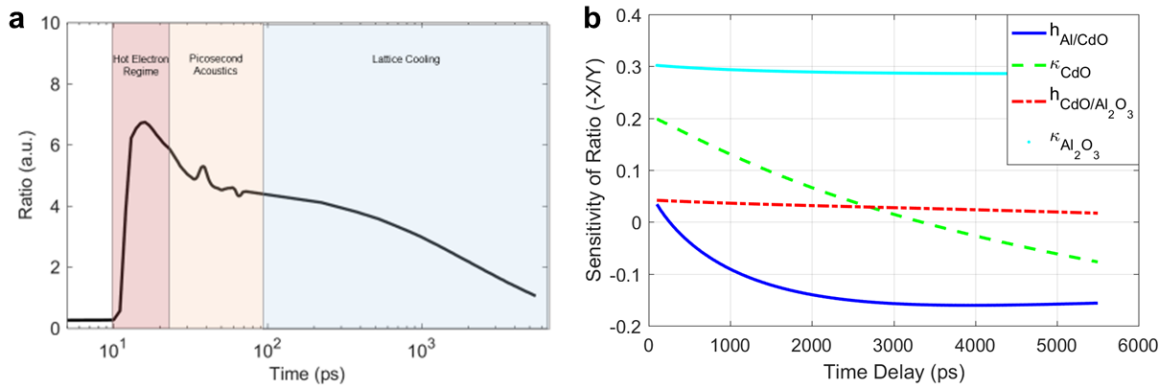

Figure S1. a) Example of a TDTR data of CdO. At relatively short pump-probe delay times (up until ~10 ps after pulse excitation), the electrons are photo-excited and begin to thermalize with the lattice. Between 10-100 ps, we can use the picosecond acoustics signatures to measure the Al transducer thickness. Our thermal conductivity results are determined from fitting TDTR data at pump-probe delay times after ~100 ps. b) Sensitivity of our thermal model to various thermophysical parameters of our Al/CdO/sapphire samples.

S2. Negligible effects of changing dislocation densities on CdO thermal conductivity and thermal boundary conductances

We confirm that dislocation profile and the backside thermal boundary conductance do not influence our measurements by analysis of a series of thin films of CdO on MgO substrates. Using the processing techniques described in the manuscript, we fabricated CdO films of thickness 1.0 nm, 1.7 nm, 3.0 nm, 5.5 nm, 7.7 nm, and 9.0 nm. These film thicknesses were verified as part of a TEM study conducted on these films[13]. In order to understand the impact of varying film thickness and its microstructural consequences on our measurement, we use Time Domain Thermoreflectance (TDTR) to measure the thermal conductance across these films as well as the thermal conductivity of the MgO substrate which they are grown on. For these measurements, we use a 53 ± 3 nm Pt transducer and analyze the films using a "2-Layer" model for the thermal diffusion of our laser heating.[12] This model fits the thermal conductance across the Pt-CdO boundary, CdO thin film, and CdO-MgO boundary as one "Film + Boundary Thermal Conductance". The other free parameter in our TDTR fitting is the substrate thermal conductivity. Both of these parameters are shown in Fig. S2. There is no significant variation in either parameter with CdO film thickness. In previous work, we have shown that the lattice mismatch between the CdO and MgO in these films induces a varying degree of misfit dislocations in higher density on the thinner films and lower density on the thicker films.[13] Thus the lack of thickness dependence demonstrates that any changes in dislocation densities in the CdO films or MoDECs will not impact our measured thermal conductivities. Furthermore, by comparison of the MgO substrate measured thermal conductivity to literature values,[14] we verify the validity of this analysis on these samples.

In order to further verify that the change in defect morphology in these films and at the CdO/MgO interface
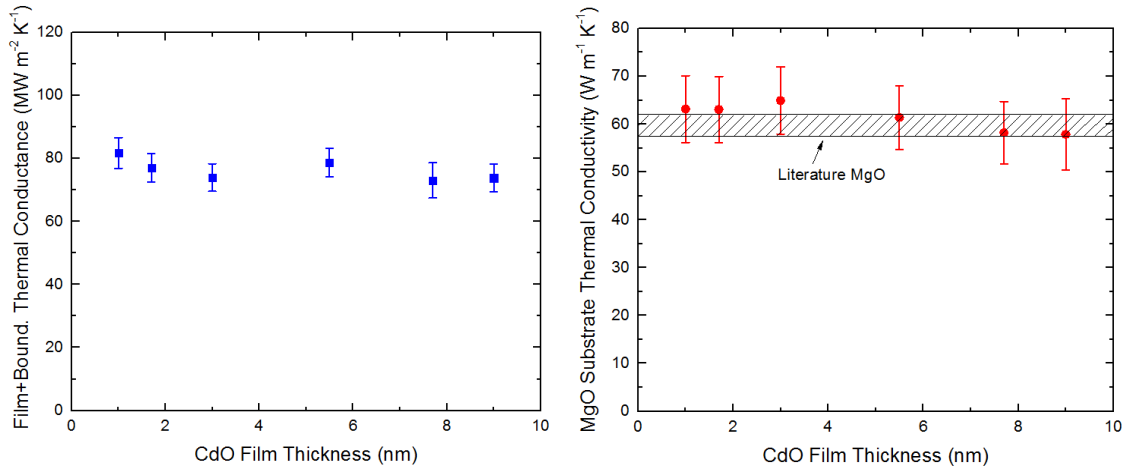

Figure S2. (left) Thermal conductance measured across the CdO film and its associated thermal boundary conductances and (right) substrate thermal conductivity for varying thicknesses of CdO thin films on MgO substrates. The increase in CdO film thickness corresponds to a corresponding increase in dislocation density,[13] and thus the lack of thickness dependence demonstrates that any changes in dislocation densities in the CdO films or MoDECs will not impact our measured thermal conductivities.

is not affecting our measurements, we conducted TDTR measurements on these thin CdO samples over a range of temperatures. Thermal transport verses temperature allows us to understand the extent of our sensitivity to these defects and interfaces as these effects become particularly relevant at low temperatures.[15] Shown in Fig. S3, there is no significant change in the measured thermal conductance (thermal conductance across the CdO films including its thermal boundary conductances associated with each interface) over temperature between the thinnest and thickest films of this set of samples. Between the full set of varying thickness CdO films, and their respective differences in defect structure at the film boundaries, and the

uniformity of behavior over temperature, it is clear that our measurement is not sensitive to any changes in dislocation density at the boundaries between the CdO and the MgO.
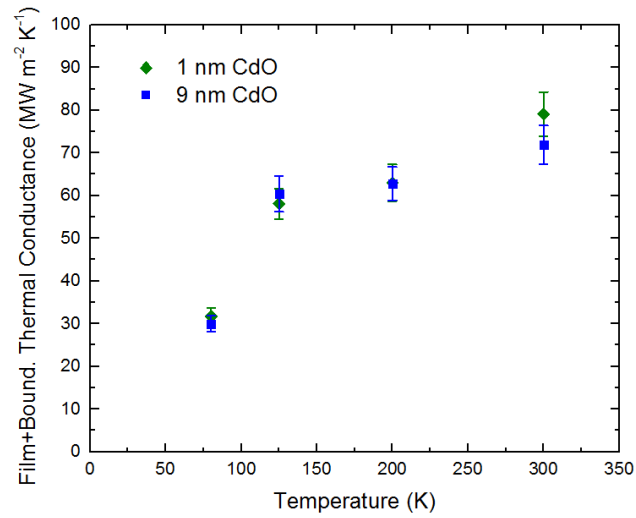

Figure S3. Thermal conductance across CdO film as a function of temperature for the thinnest and thickest CdO films. The thermal conductance reported here includes the thermal conductance across the CdO film, and each of its interfaces (Al/CdO and CdO/MgO).

S3. Negligible size effects in the thermal conductivity of CdO films and validation of interpretation using a series resistor model to interpret thermal transport in MoDECs

In the main manuscript, we reported on the thermal conductivity MoDECs with nominal thicknesses of 180 nm. We analyzed these data using a cylindrically symmetric, multilayer heat conduction model,[5, 16-18] which fundamentally assumes diffusive thermal transport in the MoDECs. Several previous works have suggested that if the length scale of ballistic thermal transport (e.g., the phonon mean free paths) in a material exceeds a measurement length scale during a modulated thermoreflectance experiment, then the measured data represent a combination of ballistic and diffusive thermal transport,[19-24] and thus the use of a diffusive heat equation to analyze the TDTR is incorrect.[21] In our experiments, the limiting length scale is governed by the thermal penetration depth, δ, since our pump and probe spot sizes are much larger than δ. The thermal penetration depth in our TDTR experiments is estimated as $\delta = (\kappa/(\pi C f))^{1/2}$, where κ is the thermal conductivity, C is the heat capacity, and f is the pump modulation frequency during a TDTR experiment. For the MoDECs studied in this work, the thermal penetration depths at an 8.8 MHz modulation frequency range from ~340 – 420 nm, depending on the thermal conductivity of the MoDECs. These thermal penetration depths are larger than the thickness of the MoDECs, and thus our use of a diffusive thermal transport model to analyze our TDTR data is acceptable.

Once determining the thermal conductivity of the MoDECs, we then interpret the experimental data based on a series resistor model (Eqs. 1 and 2 in the main manuscript). This approach implies that the MoDEC thicknesses are than the mean free paths in the MoDECs. In fact, recent first-principles calculations of the thermal conductivity of CdO by Lindsay and Parker[25] suggest that phonons with mean free paths ranging as long as 500 nm can contribute to the lattice thermal conductivity of CdO. However, also as noted by Lindsay and Parker, most likely the phonon mean free paths that contribute to the phonon thermal conductivity of CdO will be shorter than that predicted by the first-principled calculations of the perfect CdO crystal due to lattice distortions around defects that are intrinsic to CdO (e.g., oxygen vacancies).[26-27] Thus, since the MoDECs studied in this work have total thicknesses of ~180 nm, the above discussion suggests that the phonon mean free paths in the CdO studied in our present work could be on the order of the film thickness. To assess this, we turn to additional experimental testing to address the potential of ballistic transport of phonons with mean free paths exceeding the thickness of the MoDECs contributing to thermal conductivity.

To test if we expect phonon size effects and the presence of ballistic transport in our MoDECs, we conduct an additional study of the thermal conductivity of doped CdO films as function of film thickness. We grow a series of In or F doped CdO films with carrier concentrations around $6x10^{19}$ cm^{-3} on single crystal sapphire and MgO substrates, with CdO film thickness ranging from 70 – 553 nm. The thermal conductivities of these CdO films, as measured via TDTR, are shown in Fig. S4. Within uncertainty, we do not observe any size effects in the thermal conductivity of these films, indicating that the ballistic length scales of the heat carrying phonons are less than the film thickness considered in our work. We note that for the thinnest films studied in this size effect series, the uncertainties in the reported thermal conductivities are large due to the thermal boundary resistances at both metal/CdO and CdO/substrate interfaces. Regardless, for CdO film thicknesses on the order of and thicker than the MoDEC thicknesses, we do not observe any pronounced dependence of the thermal conductivity on film thickness, indicating diffusive thermal transport and thus supporting our use of the series resistor model in our analysis.
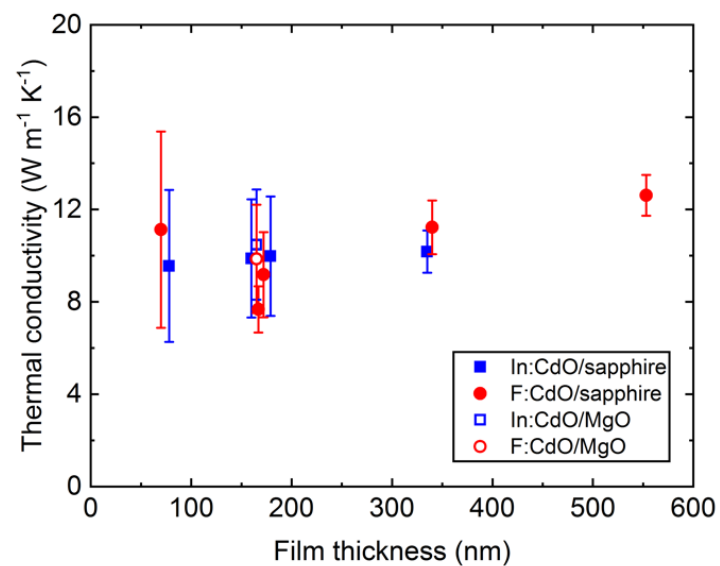
Figure S4. Thermal conductivity as a function of thickness In or F doped CdO films with carrier concentrations around 6x10^{19} cm^{-3} on single crystal sapphire and MgO substrates.

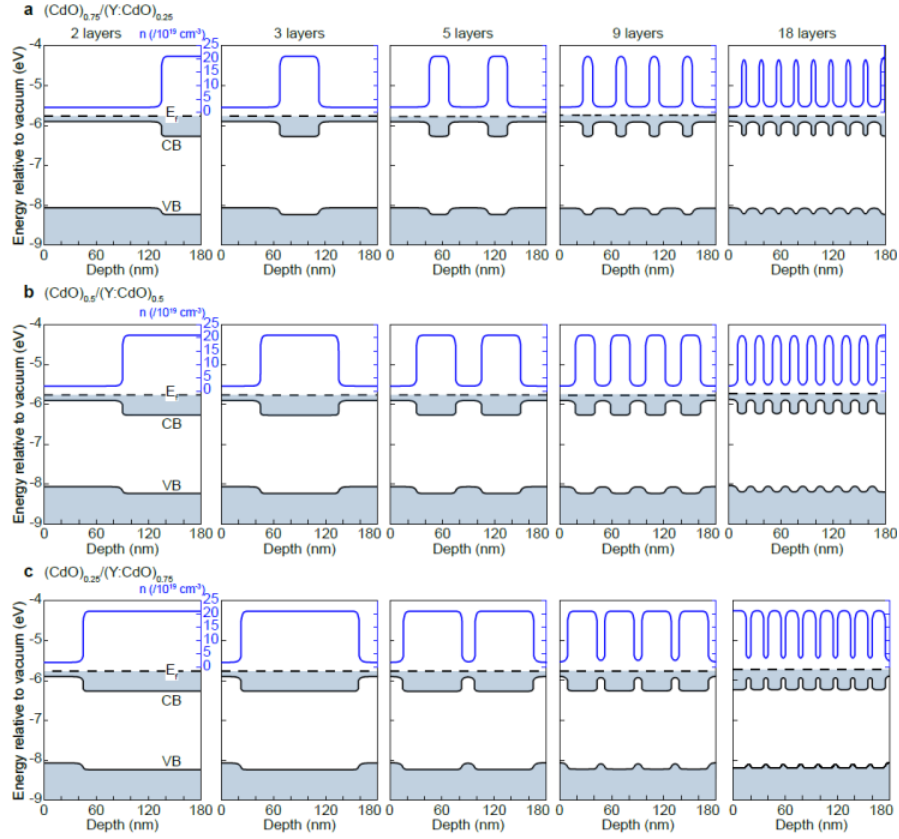# S4. Spatial segregation of free carriers in MoDECs

Figure S5. Calculated energy potentials of the conduction and valence bands, and carrier concentration as a function of depth in the three series of MoDECs series. These were created with COMSOL Multiphysics®.

To confirm that the free carriers remain spatially separated consistent with the modulated dopant profiles in the MoDECs, we used a finite-element solver (COMSOL Multiphysics, v.5.3, Semiconductor Module) to solve Poisson's equation in 1D for i-CdO/Y:CdO multilayers as studied in the main text. This allowed us to calculate the valence band maximum, conduction band minimum, Fermi level, and carrier concentration as a function of film depth for each MoDEC, based on the nominal doping levels and thicknesses of each layer in the MoDEC samples. The results (Fig. S4) show that the equilibrium free carrier density profile throughout the film largely resembles the starting simulated analytic doping profile, supporting our assertion that the free carriers are spatially localized within the MoDEC layers. The material-specific parameters (assumed from Supplementary Refs. 28-30) for the simulation are given in Table S1 below.

Table S1: Material-specific simulation parameters in COMSOL

Layer	Free carrier density	Band gap	Electron affinity	Electron effective mass	Static dielectric constant
i-CdO	1.9×10^{19} cm^{-3}	2.16 eV	5.9 eV	0.18	22
Y:CdO	2.1×10^{20} cm^{-3}	1.96 eV	6.1 eV	0.25	22

S5. Multilayered Hall effect measurement model

Hall effect measurement data from multilayered samples with top contacts, such as our MoDECs, can be analyzed in terms of a summation over all individual layers (Figure S6).[31-32] Assuming a square-shaped sample (our samples are 10x10 mm) Each ith layer has an internal resistance:

$$R_i = \frac{1}{d_i \sigma_i} = \frac{1}{d_i e n_i \mu_i}$$

where d_i is the thickness of layer i, n_i is the electron concentration in layer i, and μ_i is the Hall mobility in layer i.
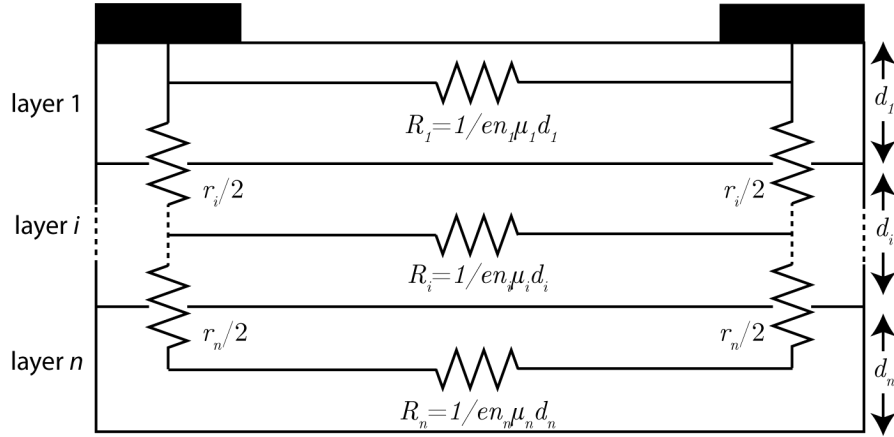

Figure S6. Schematic of multilayer model for Hall effect measurements of MoDECs.

The measured carrier concentration n_{tot} and Hall mobility μ_{tot} from the full stack of n layers are described by the following equations:[31]

$$\sigma_{\text{tot}} d_{\text{tot}} = e n_{\text{tot}} \mu_{\text{tot}} d_{\text{tot}} = \sum_i^n e n_i \mu_i d_i\, t_i$$

$$\mu_{\text{tot}} \sigma_{\text{tot}} d_{\text{tot}} = e n_{\text{tot}} \mu_{\text{tot}}^2 d_{\text{tot}} = \sum_i^n e n_i \mu_i^2 d_i\, t_i^2$$

Here, t_i is a coupling constant that describes the resistance associated with the interface between layers i and i-1. The equation describing t_i is given by:

$$t_i = \frac{R_i}{r_i + R_i}$$

where r_i is the interface resistance. If $t_i = 1$, the layers are perfectly electronically coupled with no interfacial resistance. If $t_i < 1$, there is an electronic resistance to charge transport across the interface. The situation in which $t_i > 1$ is unphysical and instead implies that the mobility in one of the layers on either side of the interface has an increased conductivity, which must come from an increase in electronic mobility.[32]

Figure S7 shows the Hall effect-measured total carrier concentration of each of the MoDECs as a function of the relative volume of Y:CdO in the stack (i.e., 0 = fully intrinsic, 0.25 = (CdO)$_{0.75}$/(Y:CdO)$_{0.25}$, etc.) All of the MoDECs, regardless of the relative volume of Y:CdO or the number of layers, are well described by a multilayered model where $t_i = 1$ and in which the electron concentration is simply given by the average carrier concentration based on the relative volumes of i-CdO and Y:CdO. This already suggests that all of the layers in the MoDECs are electronically coupled and respond to the Hall effect measurement.
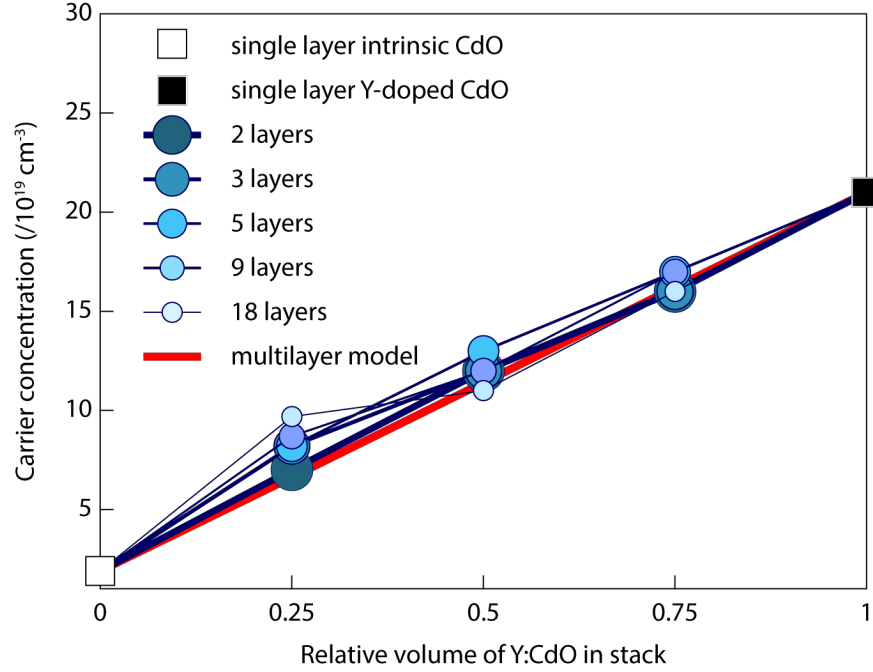
Figure S7. Free carrier concentration of each MoDEC sample as measured by the Hall effect. The average free carrier concentration, based on the relative volume of Y:CdO in the stack, is plotted as a thick red line.

Figure S8 displays the electronic Hall mobility of the MoDEC samples as a function of relative Y:CdO volume. Critically, nearly every MoDEC sample has an enhanced electronic mobility relative to the both of the i-CdO and Y:CdO endmembers/constituents. This would require coupling constants $t_i > 1$ in our multilayer model, with a maximum $t_i = 1.17$ in the $(CdO)_{0.75}/(Y:CdO)_{0.25}$ MoDECs. This necessarily means that the mobility of one or both i-CdO and Y:CdO constituents is enhanced, with the average mobility enhancement over the whole stack reaching up to 17%. This could result from three possibilities: 1) Both constituents simultaneously enjoy a mobility boost of 17%; 2) The i-CdO constituent's mobility is increased by 68% (0.17/0.25); 3) The Y:CdO constituent's mobility is increased by 23% (0.17/0.75). As discussed in the main text, we speculate that option 2 is the most likely, and that the i-CdO mobility is locally enhanced by charge transfer from Y:CdO, which neutralizes oxygen vacancy defects. Indeed, our multilayer model with $t_i = 1$ and an increased i-CdO mobility of 596 cm²/V·s qualitatively matches our electronic mobility trends.
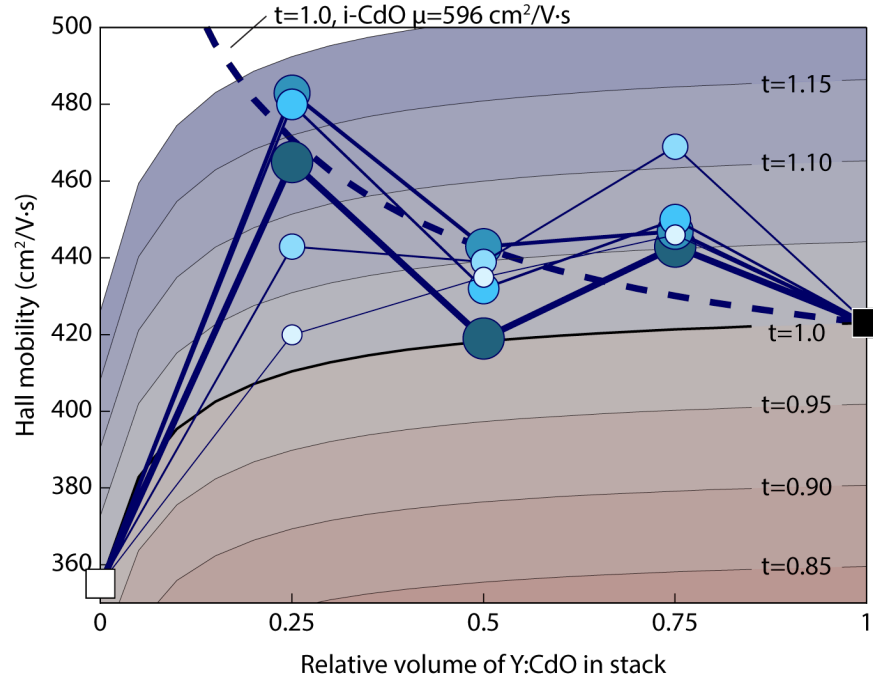
Figure S8. Measured full stack Hall mobility of each MoDEC. The colored contours represent the multilayer model-predicted Hall mobility for the full stack given differing coupling parameters t_i. The thick dashed blue line is the multilayer model-predicted Hall mobility for the full stack, given $t_i = 1$ and an i-CdO layer mobility of 596 cm²/V·s.

S6. Reflectivity measurements of MoDEC multilayers

To ensure that Y dopants and free carriers are segregated as expected and as modeled in Figure 2b of the main text, we measured the mid-infrared reflectivity spectra of MoDEC samples. We note that measurements of mid-infrared reflectivity spectra are a common technique to characterize all manner of optical behaviors of materials (e.g., band gaps, phonons, and free-carrier oscillations), including those in thin films and superlattices.[33-38] Figure S9 presents an example reflectivity spectrum of a 5-layer MoDEC taken at 65° incidence, presented as the ratio of reflected p-polarized to s-polarized light. The two distinct reflectivity-edge features at 3800 cm^{-1} and 2200 cm^{-1} are a clear signature of two separate/discrete populations of differing free carrier concentration within the MoDEC.
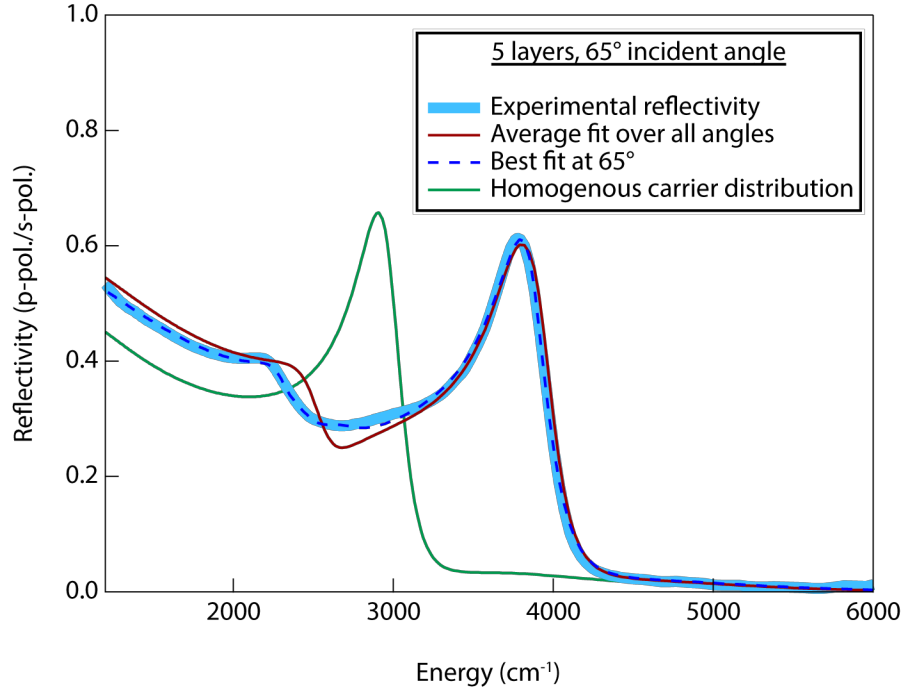

Figure S9. Reflectivity spectrum of a representative 5-layer MoDEC, presented as the ratio of reflected p-polarized light to s-polarized light at 65° incident angle (thick, light blue line). The best fit to the data at this angle using the multilayered transfer matrix model is plotted as a dashed dark blue thin line. The thin red line is the simulated reflectivity spectrum using the best fits averaged over all the incident angles. The thin green line is the simulated reflectivity spectrum of a single layer with a homogenous free carrier concentration.

Also plotted are fits to the data, which we performed using a transfer matrix model to calculate the Fresnel reflection and transmission coefficients at each i-CdO/Y:CdO interface. The dielectric functions of the i-CdO and Y:CdO layers are simulated using the Drude model:

$$\varepsilon(\omega) = \varepsilon_\infty - \frac{\omega_p^2}{\omega^2 + i\gamma\omega}$$

$$\omega_p^2 = \frac{ne^2}{m^*\varepsilon_0}$$

where ε_∞ is the high-frequency dielectric constant, ω_p is the plasma frequency, γ is the damping frequency, n is the free carrier concentration, and m^* is the effective mass.

Both the best fit at 65° and the average fit over all the measured angles (50° – 80° by 5° increments) describe the reflectivity data well. Importantly, both fits contain 3 layers with low carrier concentration (6 – 7×10^{19} cm^{-3}) and 2 layers with high carrier concentration (~2.3×10^{20} cm^{-3}). See Tables S2 and S3, below, for the fitted values. We note that our fitting scheme is rather basic at this time, so the fitted parameters in Tables S2 and S3 are not necessarily quantitative. We can nonetheless definitively say that the i-CdO and Y:CdO

layers maintain their individual character, with discrete and different free carrier concentrations. Finally, a complementary simulation of a single CdO layer with a homogenous average carrier concentration of 1.2×10^{20} cm^{-3} is also plotted for reference (thin green line). This simulated reflectivity spectrum is a poor match for our experimental data, as it displays only one reflection edge that does not match the energy of either reflection edge in the experimental data.

Table S2. Best fit parameters for infrared reflectivity of 5-layer MoDEC, 65° incident angle.

Layer	Thickness	ε_∞	n (cm^{-3})	μ (cm^2/V·s)	Eff. mass
i-CdO	15 nm	5.7	6.6×10^{19}	176 cm^2/V·s	0.17
Y:CdO	54 nm	4.9	2.3×10^{20}	154 cm^2/V·s	0.28
i-CdO	15 nm	5.7	7.6×10^{19}	138 cm^2/V·s	0.16
Y:CdO	47 nm	5.2	2.3×10^{20}	87 cm^2/V·s	0.27
i-CdO	21 nm	5.6	6.6×10^{19}	225 cm^2/V·s	0.20

Table S3. Average fit parameters for infrared reflectivity of 5-layer MoDEC, 50 – 80° incident angle.

Layer	Thickness	ε_∞	n	μ	Eff. mass
i-CdO	17 ± 4 nm	5.6 ± 0.1	$7.1 \times 10^{19} \pm 8.5 \times 10^{18}$	160 ± 53	0.17 ± 0.02
Y:CdO	50 ± 7 nm	5.1 ± 0.1	$2.3 \times 10^{20} \pm 7.1 \times 10^{18}$	160 ± 24	0.26 ± 0.01
i-CdO	21 ± 6 nm	5.6 ± 0.1	$7.2 \times 10^{19} \pm 1.4 \times 10^{19}$	186 ± 63	0.18 ± 0.03
Y:CdO	46 ± 4 nm	5.2 ± 0.1	$2.2 \times 10^{20} \pm 8.6 \times 10^{18}$	129 ± 33	0.26 ± 0.01
i-CdO	23 ± 6 nm	5.6 ± 0.1	$7.1 \times 10^{19} \pm 3.4 \times 10^{18}$	165 ± 42	0.18 ± 0.02

We note that diffusion in CdO is vacancy-mediated,[39] and, due to the close-packed rocksalt structure, there is not room for interstitials (especially considering our epitaxial films with the high crystallographic quality shown in Fig. 1 of the main manuscript). At the sputtering temperature of 455 °C the lattice diffusion constant is estimated to be 8.8×10^{-22} cm^2 s^{-1}, for a diffusion length of 0.025 nm, so the Y atoms are not diffusing out of their respective layers during growth. One might expect diffusion during the 700 °C anneal, where the diffusion constant is higher (8.08×10^{-15} cm^2 s^{-1}). However, because diffusion in CdO is vacancy-mediated, diffusion of Y dopants out of their respective layers during this step would require a significant amount of Cd vacancies. We showed in our previous work[26] that cadmium vacancies are not the dominant defect in doped CdO as the formation energies for V_{Cd} are generally large, and metal vacancies are unlikely to be the prevalent defect. A lack of cadmium vacancies will prevent Y dopants from diffusing out of their layers. Indeed, we see that this is true with our above-discussed IR reflectivity data.

Supporting Information References

1. Ghotbi, M.; Ebrahim-Zadeh, M.; Majchrowski, A.; Michalski, E.; Kityk, I. V., High-Average-Power Femtosecond Pulse Generation in the Blue Using BiB_3O_6. *Optics Letters* **2004**, *29*, 2530--2532.
2. Wang, L.; Cheaito, R.; Braun, J. L.; Giri, A.; Hopkins, P. E., Thermal Conductivity Measurements of Non-Metals Via Combined Time- and Frequency-Domain Thermoreflectance without a Metal Film Transducer. *Review of Scientific Instruments* **2016**, *87*, 094902.
3. Thomsen, C.; Strait, J.; Vardeny, Z.; Maris, H. J.; Tauc, J.; Hauser, J. J., Coherent Phonon Generation and Detection by Picosecond Light Pulses. *Physical Review Letters* **1984**, *53*, 989-992.
4. Thomsen, C.; Grahn, H. T.; Maris, H. J.; Tauc, J., Surface Generation and Detection of Phonons by Picosecond Light Pulses. *Physical Review B* **1986**, *34*, 4129-4138.
5. Cahill, D. G., Analysis of Heat Flow in Layered Structures for Time-Domain Thermoreflectance. *Review of Scientific Instruments* **2004**, *75*, 5119-5122.
6. Schmidt, A. J., Pump-Probe Thermoreflectance. *Annual Review of Heat Transfer* **2013**, *16*, 159-181.
7. Cadmium Oxide (Cdo) Debye Temperature, Heat Capacity, Melting Point, Density. In *II-VI and I-VII Compounds; Semimagnetic Compounds*, Madelung, O.; Rössler, U.; Schulz, M., Eds. Springer Berlin Heidelberg: Berlin, Heidelberg, 1999; pp 1-3.
8. Touloukian, Y. S.; Buyco, E. H., *Thermophysical Properties of Matter - Specific Heat: Metallic Elements and Alloys*; New York, IFI/Plenum, 1970; Vol. 4.
9. Touloukian, Y. S.; Powell, R. W.; Ho, C. Y.; Klemens, P. G., *Thermophysical Properties of Matter - Specific Heat: Nonmetallic Solids*; New York, IFI/Plenum, 1970; Vol. 5.
10. Gutowski, J., Cdo: Heat Capacity. In *New Data and Updates for IV-IV, III-V, II-VI and I-VII Compounds, Their Mixed Crystals and Diluted Magnetic Semiconductors*, Rössler, U., Ed. Springer Berlin Heidelberg: Berlin, Heidelberg, 2011; pp 323-323.
11. Gundrum, B. C.; Cahill, D. G.; Averback, R. S., Thermal Conductance of Metal-Metal Interfaces. *Physical Review B* **2005**, *72*, 245426.
12. Liu, J.; Zhu, J.; Tian, M.; Gu, X.; Schmidt, A.; Yang, R., Simultaneous Measurement of Thermal Conductivity and Heat Capacity of Bulk and Thin Film Materials Using Frequency-Dependent Transient Thermoreflectance Method. *Review of Scientific Instruments* **2013**, *84*, 034902.
13. Grimley, E. D.; Sachet, E.; Donovan, B. F.; Hopkins, P. E.; Maria, J. P.; LeBeau, J. M., Observing Misfit Dislocation Interactions across Thin Film Oxide Heterostructures. *Microscopy and Microanalysis* **2016**, *22*, 1506-1507.
14. Slack, G. A., Thermal Conductivity of MgO, Al_2O_3, $MgAl_2O_4$, and FeO_4 Crystals from 3 to 300 K. *Physical Review* **1962**, *126*, 427--441.
15. Srivastava, G. P., *The Physics of Phonons*; Taylor and Francis: New York, 1990.
16. Hopkins, P. E.; Serrano, J. R.; Phinney, L. M.; Kearney, S. P.; Grasser, T. W.; Harris, C. T., Criteria for Cross-Plane Dominated Thermal Transport in Multilayer Thin Film Systems During Modulated Laser Heating. *Journal of Heat Transfer* **2010**, *132*, 081302.
17. Braun, J. L.; Hopkins, P. E., Upper Limit to the Thermal Penetration Depth During Modulated Heating of Multilayer Thin Films with Pulsed and Continuous Wave Lasers: A Numerical Study. *Journal of Applied Physics* **2017**, *121*, 175107.
18. Braun, J.; Szwejkowski, C. J.; Giri, A.; Hopkins, P. E., On the Steady-State Temperature Rise During Laser Heating of Multilayer Thin Films in Optical Pump-Probe Techniques. *Journal of Heat Transfer* **2018**, *140*, 052801.
19. Chen, L.; Braun, J. L.; Donovan, B. F.; Hopkins, P. E.; Poon, S. J., Ballistic Transport of Long Wavelength Phonons and Thermal Conductivity Accumulation in Nanograined Silicon-Germanium Alloys. *Applied Physics Letters* **2017**, *111*, 131902.
20. Koh, Y. K.; Cahill, D. G., Frequency Dependence of the Thermal Conductivity of Semiconductor Alloys. *Physical Review B* **2007**, *76*, 075207.
21. Wilson, R. B.; Cahill, D. G., Anisotropic Failure of Fourier Theory in Time-Domain Thermoreflectance Experiments. *Nature Communications* **2014**, *5*, 5075.

22. Siemens, M. E.; Li, Q.; Yang, R.; Nelson, K. A.; Anderson, E. H.; Murnane, M. M.; Kapteyn, H. C., Quasi-Ballistic Thermal Transport from Nanoscale Interfaces Observed Using Ultrafast Coherent Soft X-Ray Beams. *Nature Materials* **2010**, *9*, 26--30.

23. Minnich, A. J.; Johnson, J. A.; Schmidt, A. J.; Esfarjani, K.; Dresselhaus, M. S.; Nelson, K. A.; Chen, G., Thermal Conductivity Spectroscopy Technique to Measure Phonon Mean Free Paths. *Physical Review Letters* **2011**, *107*, 095901.

24. Regner, K. T.; Sellan, D. P.; Su, Z.; Amon, C. H.; McGaughey, A. J. H.; Malen, J. A., Broadband Phonon Mean Freee Path Contributions to Thermal Conductivity Measured Using Frequency Domain Thermoreflectance. *Nature Communications* **2013**, *4*, 1640.

25. Lindsay, L.; Parker, D. S., Calculated Transport Properties of Cdo: Thermal Conductivity and Thermoelectric Power Factor. *Physical Review B* **2015**, *92*, 144301.

26. Sachet, E.; Shelton, C.T.; Harris, J.S.; Gaddy, B.E.; Irving, D.L.; Curtarolo, S.; Donovan, B.F.; Hopkins, P.E.; Sharma, P.A., Sharma, A.L.; Ihlefeld, J.F.; Franzen, S.; Maria, J.-P., Dysprosium-Doped Cadmium Oxide as a Gateway Material for Mid-Infrared Plasmonics. *Nature Materials* **2015**, *14*, 414-420.

27. Donovan, B. F.; Sachet, E.; Maria, J.-P.; Hopkins, P. E., Interplay between Mass-Impurity and Vacancy Phonon Scattering Effects on the Thermal Conductivity of Doped Cadmium Oxide. *Applied Physics Letters* **2016**, *108*, 021901.

28. Speaks, D. T.; Mayer, M. A.; Yu, K. M.; Mao, S. S.; Haller, E. E.; Walukiewicz, W., Fermi Level Stabilization Energy in Cadmium Oxide. *Journal of Applied Physics* **2010**, *107*, 113706.

29. Rueben, J. M.; Yuankun, Z.; André, A., Determining the Nonparabolicity Factor of the Cdo Conduction Band Using Indium Doping and the Drude Theory. *Journal of Physics D: Applied Physics* **2012**, *45*, 425302.

30. Yuankun, Z.; Rueben, J. M.; Jiaqi, Z.; Jiecai, H.; André, A., Dopant-Induced Band Filling and Bandgap Renormalization in CdO:In Films. *Journal of Physics D: Applied Physics* **2013**, *46*, 195102.

31. Arnaudov, B.; Paskova, T.; Evtimova, S.; Valcheva, E.; Heuken, M.; Monemar, B., Multilayer Model for Hall Effect Data Analysis of Semiconductor Structures with Step-Changed Conductivity. *Physical Review B* **2003**, *67*, 045314.

32. Nishitani, J.; Yu, K. M.; Walukiewicz, W., Charge Transfer and Mobility Enhancement at CdO/SnTe Heterointerfaces. *Applied Physics Letters* **2014**, *105*, 132103.

33. Talwar, D.N.; Yang, T.-R.; Feng, Z.C.; Becla, P., Infrared reflectance and transmission spectra in II-VI alloys and superlattices. *Physical Review B* **2011**, *84*, 174203.

34. Maslin, K.A.; Parker, T.J.; Raj, N.; Tilley, D.R.; Dobson, P.J.; Hilton, D.; Foxon, C.T.B., Far infrared reflectivity of semiconductor superlattice and multi-quantum well structures. *Solid State Communications* **1986**, *60*, 461-464.

35. Webster, P. T.; Riordan, N.A.; Liu, S.; Steenbergen, E.H.; Synowicki, R.A.; Zhang, Y.-H.; Johnson, S.R., Absorption properties of type-II InAs/InAsSb superlattices measured by spectroscopic ellipsometry. *Applied Physics Letters* **2015**, *106*, 061907.

36. Šik, J.; Schubert, M., Band-gap energies, free carrier effects, and phonon modes in strained GaNAs/GaAs and GaNAs/InAs/GaAs superlattice heterostructures measured by spectroscopic ellipsometry. *Journal of Applied Physics* **2001**, *89*, 294-305.

37. Ashkenov, N.; Mbenkum, B.N.; Bundesmann, C.; Riede, V.; Spemann, D.; Kaidashev, E.M.; Kasic, A.; Schubert, M.; Grundmann, M., Infrared dielectric functions and phonon modes of high-quality ZnO films. *Journal of Applied Physics* **2003**, *93*, 126-133.

38. Holden, T.; Habermeier, H.-W.; Cristiani, G.; Golnik A.; Boris, A.; Pimenov, A.; Humlicek, J.; Lebedev, O.I.; Van Tendeloo, G.; Keimer, B.; Bernhard, C., Proximity induced metal-insulator transition in $YBa_2Cu_3O_7/La_{2/3}Ca_{1/3}MnO_3$ superlattices. *Physical Review B* **2004**, *69*, 064505.

39. Haul, R.; Just, D., Disorder and Oxygen Transport in Cadmium Oxide. *Journal of Applied Physics* **1962**, *33*, 487-493.